

# 中国激光

## 基于超表面波带片的远场偏振全息加密

夏天, 谢振威\*, 袁小聪\*\*

深圳大学纳米光子学研究中心, 微纳光电子学研究院, 异质异构集成全国重点实验室, 广东 深圳 518060

**摘要** 超表面是一种具有灵活的偏振操纵功能的新型材料。为了获得远场偏振全息图像, 通常需要添加透镜等光学元件。笔者利用超表面波带片的灵活偏振操纵及聚焦功能实现了一种新颖的远场偏振全息加密技术。在该技术中, 两个自旋复用的超表面波带片被集成到单个介质超表面器件中, 其中超表面的振幅(右旋圆偏振转化率)用来编码奇数和偶数环形区域的波带片, 而其相位调制则用来编码透射右旋圆偏振光和左旋圆偏振光的两个全息图。此外, 二维码(QR码)和振幅型/相位型全息图用于进一步隐藏加密信息, 以提高信息的安全性。所提加密技术有望进一步提升数据安全性和隐私保护水平, 推动光学信息加密和高密度数据存储等领域的技术发展。

**关键词** 表面光学; 超表面波带片; 远场偏振全息加密; QR码; 全息

中图分类号 O436 文献标志码 A

DOI: 10.3788/CJL230695

### 1 引言

超表面因能够任意调控波前而被广泛认为是传统光学元件的潜在替代品。可重构的超表面不仅能够满足光学系统设计对小型化器件的需求, 还由于其超原子具有多种设计自由度和光场操纵自由度而在彩色打印<sup>[1-2]</sup>、光学加密<sup>[3]</sup>、超透镜<sup>[4-6]</sup>、全息术<sup>[7-11]</sup>和非线性光学<sup>[12-14]</sup>等领域具有广阔的应用前景。

光具有许多基本调控参量, 如振幅、相位、偏振、频率、入射角、轨道角动量和自旋角动量等, 其中的偏振是一个关键参量, 可用于光学信息编码、数据存储和复用传输通信等。通过控制电磁波的偏振, 超表面可以实现偏振复用和矢量超表面全息。超表面全息所需要的全息图通常通过传统的相位恢复算法来生成<sup>[15-17]</sup>。偏振全息可以通过正交或任意偏振来调节, 包括线偏振、圆偏振、椭圆偏振和多通道偏振。偏振超表面全息自提出以来, 已经取得了重大进展, 包括基于马吕斯定律<sup>[18-19]</sup>、斯托克斯矢量<sup>[20-22]</sup>和多通道复用<sup>[23-25]</sup>的技术。值得注意的是, 近些年远场偏振全息引起了研究人员的极大兴趣。超表面可以在实空间中生成二进制或灰度图像, 同时在  $k$  空间中生成偏振全息图像<sup>[26]</sup>。另外, 使用双相位方法制备的超表面可以在聚焦透镜的焦平面上产生全息图像, 该图像具有设计的偏振状态和衍射级别<sup>[27]</sup>。但是, 上述方法需要在光路中添加透镜。超表面波带片(meta-FZP)是一种新型的光学元件, 具有许多出色的特性。利用介质超表面波带片取代菲涅

耳波带片, 能够同时调节光的振幅、相位和偏振, 并且控制的偏振态能覆盖整个庞加莱球<sup>[28]</sup>。携带螺旋相位的偏振不敏感超表面波带片能够产生多个具有不同轨道角动量的涡旋光束<sup>[29]</sup>。此外, 研究人员还报道了奇偶区由不同超原子组成的太赫兹超表面波带片可以实现从任意入射偏振态到固定偏振态的转换<sup>[30]</sup>。然而, 基于超表面波带片的远场偏振全息还没有得到深入研究。

笔者提出了一种可实现远场偏振全息加密的自旋复用介质超表面, 该超表面器件由两个振幅型奇偶超表面波带片构成。奇偶超表面波带片的相位分别对应于透射的右旋和左旋圆偏振光的相位全息图。加密的全息信息只有在单个圆偏振分量被过滤后才能解密。此外, 笔者采用二维码(QR码)和振幅/相位型全息图来增强信息加密的安全性。QR码与转换的圆偏振态有关, 最终加密的信息可以使用手机相机和傅里叶变换进行解密。这些技术提高了全息加密的安全性和可靠性。

### 2 设计与理论

图 1 是超表面波带片远场偏振全息加密的原理图。奇偶数菲涅耳超表面波带片分别将入射的左旋圆偏振光(LCP)转化为右旋圆偏振光(RCP)和左旋圆偏振光。虽然不同手性的圆偏振光携带着不同的全息相位, 但它们都会在奇偶数菲涅耳波带片相同的焦平面处产生期望的 QR 码图像, 通过手机相机识别 QR 码可以获得

收稿日期: 2023-04-10; 修回日期: 2023-05-17; 录用日期: 2023-05-24; 网络首发日期: 2023-06-06

基金项目: 广东省基础与应用基础研究重大项目(2020B0301030009)、国家自然科学基金(61935013, 61975133)、深圳市科技计划基础研究重点项目(JCYJ20180507182035270, JCYJ20200109114018750)、深圳市孔雀团队项目(KQTD20170330110444030)

通信作者: \*ayst31415926@szu.edu.cn; \*\*xcyuan@szu.edu.cn

振幅型/相位型全息图,然后按照不同全息图的解密方式进行傅里叶变换就可以得到最终的加密图像。

二氧化钛椭圆柱单元的长轴为  $a$ ,短轴为  $b$ ,高度为  $h$ ( $h=1000$  nm),单元周期  $P$  为 500 nm。图 2(b)、

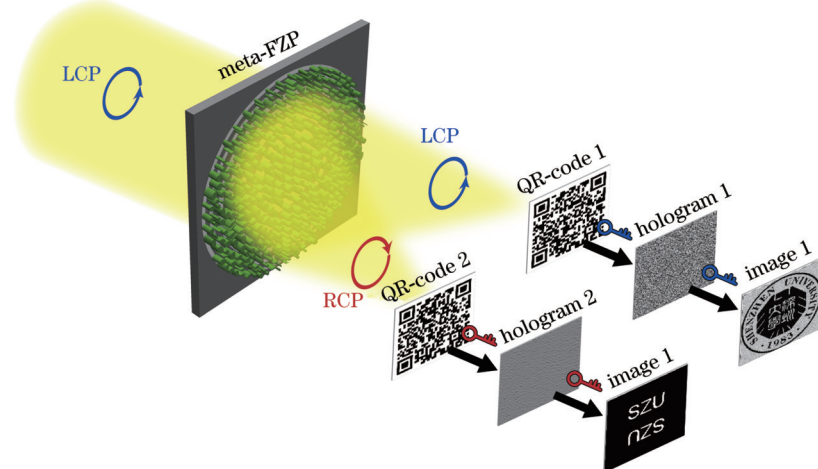


图 1 超表面波带片加密原理图

Fig. 1 Diagram of the metasurface zone plate encryption

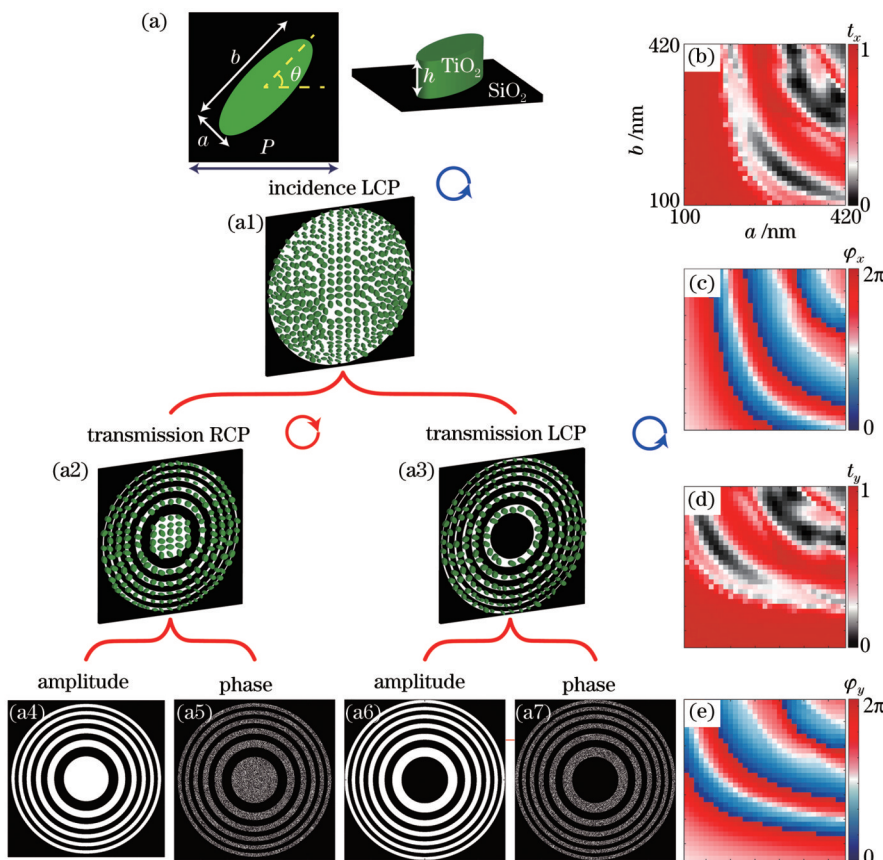


图 2 超表面波带片的调控机制。(a)超原子的俯视图和侧视图;在波长为 633 nm 的  $x$  线偏振入射光下,不同尺寸的超原子在  $x$  偏振方向的透过率分布图(b)和相位分布图(c);在波长为 633 nm 的  $y$  线偏振入射光下,不同尺寸的超原子在  $y$  偏振方向的透过率分布图(d)和相位分布图(e);在左旋圆偏振入射光下,超表面(a1)由奇数超表面波带片(a2)和偶数超表面波带片(a3)组成,其中,奇数超表面波带片的振幅和相位分别如图(a4)、(a5)所示,偶数超表面波带片振幅和相位分别如图(a6)、(a7)所示

Fig. 2 Modulation mechanism of metasurface zone plates. (a) The top and side views of the meta-atom; transmission (b) and phase (c) of the meta-atom with different sizes along  $x$ -polarization under the  $x$ -linearly polarized light with the wavelength of 633 nm; transmission (d) and phase (e) of the meta-atom with different sizes along  $y$ -polarization under the  $y$ -linearly polarized light; under the left-circularly polarized incident light, the metasurface (a1) consists of the odd metasurface zone plate (a2) and even metasurface zone plate (a3), where the amplitude and phase of the former were exhibited in Figs. (a4) and (a5) and those of the latter were exhibited in Figs. (a6) and (a7)

(d) 分别展示了入射光波长为 633 nm 时, 不同尺寸的超原子在  $x$  线偏振光和  $y$  线偏振光照射下在  $x$  偏振方向和  $y$  偏振方向的透过率, 相应的相位调制如图 2(c)、(e) 所示。如图 2(a1) 所示, 超表面菲涅耳波带片由奇数和偶数环形区域组成。合理选择相应的超表面单元, 当左旋圆偏振光照射到超表面上时, 奇数环带菲涅耳波带片区域的超表面单元可以将入射的左旋圆偏振光完全转化为右旋圆偏振光(偏振转化率为 100%), 而偶数环带菲涅耳波带片区域的超表面单元则仍然使入射光保持左旋圆偏振状态(偏振保持率为 100%, 偏振转化率为 0%)。对于图 2(a2) 中的奇数环形区域, 变换后的右旋圆偏振光的振幅等于 1; 而对于图 2(a3) 中的偶数环形区域, 变换后的左旋圆偏振光的振幅也为 1。如图 2(a4) 和图 2(a6) 所示, 奇偶环形区域的振幅分别为振幅型奇偶数菲涅耳波带片的振幅。此外, 奇数和偶数区域中的超表面单元的相位调制分别对应于透射的右旋和左旋圆偏振光的全息图。因此, 在焦平面上会形成两个圆偏振各自的全息图像。然而, 由于图像重叠, 无法识别所需的加密全息图像, 需要过滤掉右旋或左旋圆偏振部分, 以进一步解密相应的加密全息图像。当入射光具有左旋圆偏振态时, 可以使用式(1)<sup>[31]</sup> 计算超原子的输出光场  $E_{\text{out}}$ 。值得注意的是, 入射光的偏振态为左旋圆偏振, 经过超表面单元后入射光的左旋圆偏振转化为左旋圆偏振或者右旋圆偏

振, 相应的偏振态在图中利用逆时针/顺时针方向圆形箭头来表示。

$$E_{\text{out}} = \mathbf{J}(\theta)|L\rangle = \sin\left(\frac{\Delta\varphi}{2}\right)\exp(i\phi_1)|R\rangle + \cos\left(\frac{\Delta\varphi}{2}\right)\exp(i\phi_2)|L\rangle, \quad (1)$$

$$\begin{cases} \phi_1 = (\Sigma\varphi - \pi)/2 - 2\theta \\ \phi_2 = (\Sigma\varphi)/2 \\ \Sigma\varphi = \varphi_x + \varphi_y \\ \Delta\varphi = \varphi_x - \varphi_y \end{cases}, \quad (2)$$

式中:  $\mathbf{J}(\theta)$  表示琼斯矩阵;  $\phi_1$  和  $\phi_2$  分别表示透射的右旋圆偏振  $|R\rangle$  和左旋圆偏振  $|L\rangle$  的全息相位;  $\Sigma\varphi$  表示传输相位的总和;  $\theta$  表示几何相位;  $\varphi_x$  和  $\varphi_y$  分别表示  $x$  和  $y$  线偏振入射光下沿着  $x$  和  $y$  方向的透射传输相位;  $\Delta\varphi$  表示  $\varphi_x$  和  $\varphi_y$  之间的相位差。根据上述分析, 对应于透射的右旋和左旋圆偏振光的奇偶环形区域上的全息图分别具有大小为  $\pi$  和 0 的  $\Delta\varphi$  值。

### 3 结果与讨论

透射的右旋和左旋圆偏振光的编码信息分别表示在图 3 中的第一行和第二行, 图中横纵轴分别表示  $x$  和  $y$  方向的尺寸。通过 QR 码生成网站来生成由 GS 算法获得的全息图所对应的 QR 码。图 3(a1)、(a2) 中的 QR 码

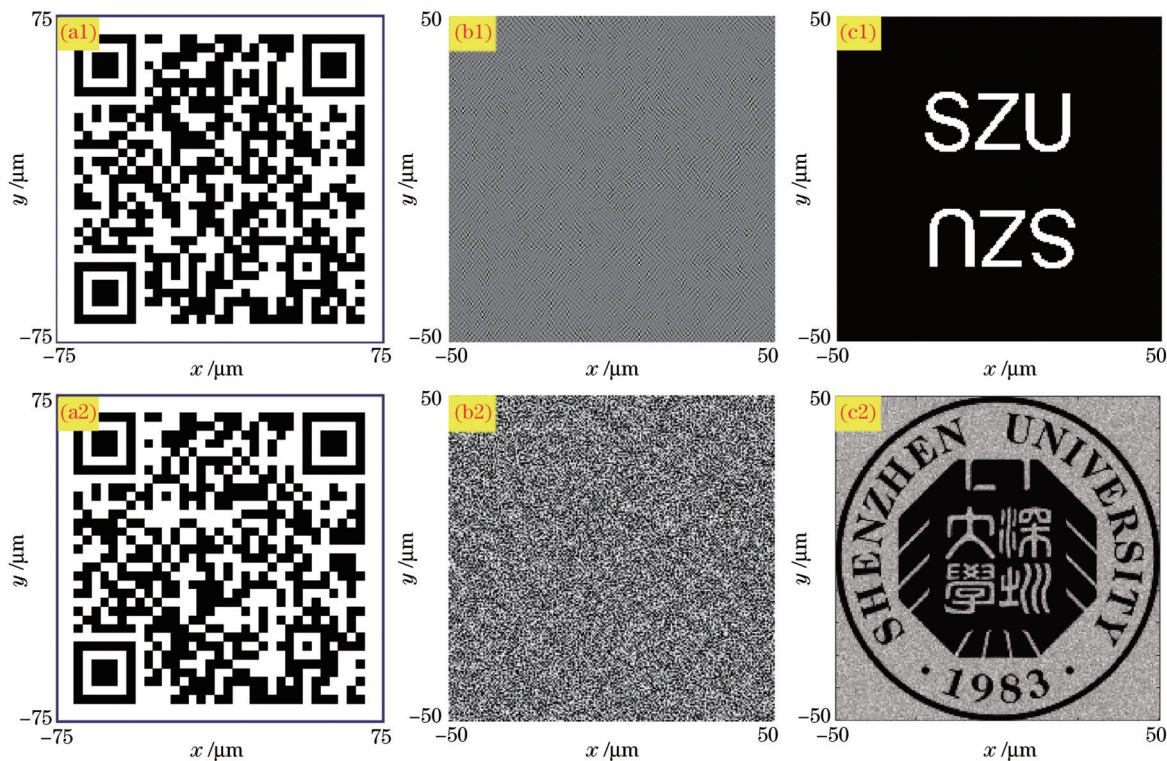


图 3 透射圆偏振光的编码信息。(a1)(a2)QR 码;(b1)QR 产生的振幅型相位型全息图;(b2)QR 产生的相位型全息图;(c1)振幅型全息图在远场模拟计算的加密强度图;(c2)相位型全息图在远场模拟计算的加密强度图

Fig. 3 Encoding information of transmitted circularly polarized light. (a1)(a2) QR codes; (b1) QR codes generated amplitude-only hologram; (b2) QR codes generated phase-only hologram; (c1) calculated encrypted intensity profile in the far field of the amplitude-only hologram; (c2) calculated encrypted intensity distribution in the far field of the phase-only hologram

分别对应于图 3(b1)中的振幅型全息图和图 3(b2)中的相位型全息图。经过傅里叶变换后,振幅型全息图产生了图 3(c1)所示的加密强度分布,而相位型全息图生成了图 3(c2)所示的加密强度分布。

图 4 中横纵轴分别表示  $x$  和  $y$  方向的尺寸。图 4(a1)、(b1) 分别是透射右旋和左旋圆偏振分量的全息图,这些图对应于奇偶环形区域的相位。虽然左旋和右旋圆偏振分量在奇偶环形区域中携带了图 4(a2)、(b2) 所示的相位,但这些相位的振幅基本为零,可以忽略不计。对于奇数区域,由式(2)和  $\Delta\phi=\pi$  得到了  $\varphi_x=\phi_2+\pi/2$ 、 $\varphi_y=\phi_2-\pi/2$  和  $\theta=(\phi_2-\phi_1)/2-\pi/4$ ,从而产生了图 4(c1)~(e1) 所示的相位图。对于偶数区域,由式

(2) 和  $\Delta\phi=0$  得到了  $\varphi_x=\phi_2$ 、 $\varphi_y=\phi_2$  和  $\theta=(\phi_2-\phi_1)/2-\pi/4$ ,从而产生了图 4(c2)~(e2) 所示的相位图。超表面上第  $n$  个环形区域的外半径  $r_n$  能通过表达式  $\sqrt{n\lambda f + \frac{n^2\lambda^2}{4}}$  计算出来。其中,  $\lambda$  和  $f$  分别表示入射光波长和菲涅耳波带片的焦长。奇偶数菲涅耳波带片的半径为 1.5 mm,其透光和非透光环形区都为 126 个,总的环形区数为 252 个,其焦距都为 14.1 mm。波长  $\lambda$  等于 633 nm,全息距离等于焦距,全息距离也为 14.1 mm。衍射效率定义为焦斑的总能量与衍射元件输入总能量的比值。本次实验中设计的奇偶数菲涅耳波带片在理想情况下的衍射效率分别为 19.27% 和 19.19%。

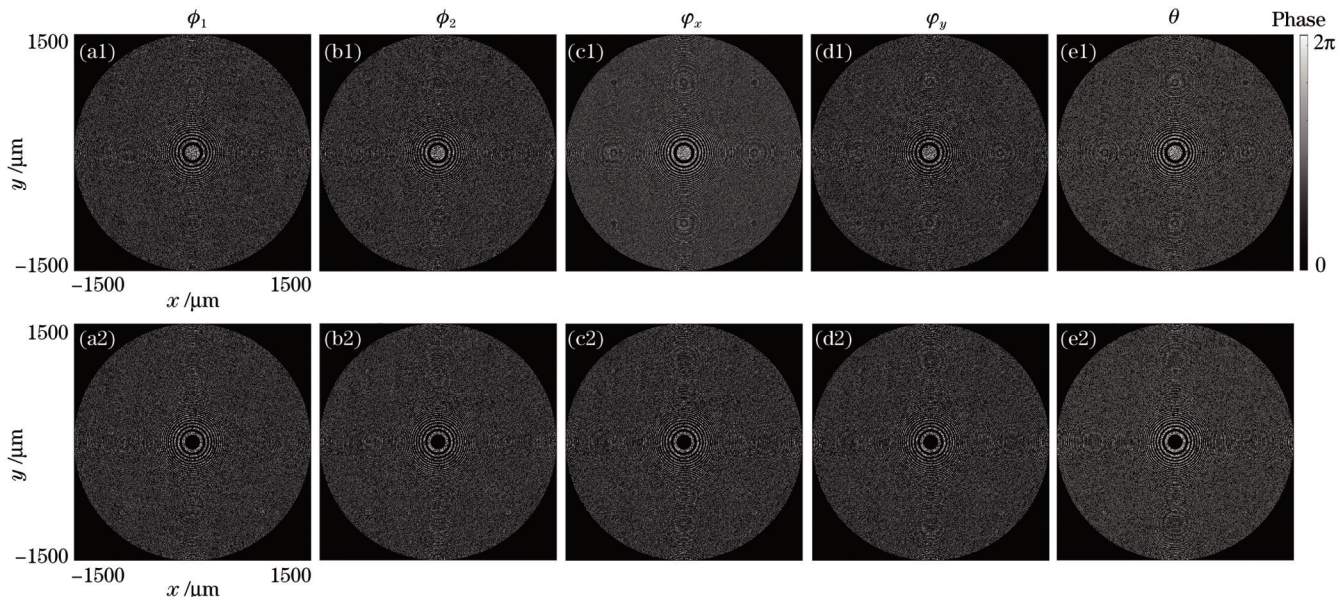


图 4 在左旋圆偏振光下,透射的右旋圆偏振光(a1)和左旋圆偏振光(b1)在奇数环形区域的全息相位,以及相对应的在  $x$  和  $y$  线偏振入射光下分别沿着  $x$  方向(c1)、 $y$  方向(d1)的传输相位及几何相位(e1)。透射的右旋圆偏振光(a2)和左旋圆偏振光(b2)在偶数环形区域的全息相位,以及相对应的在  $x$  和  $y$  线偏振入射光下分别沿着  $x$  方向(c2)、 $y$  方向(d2)的传输相位及几何相位(e2)

Fig. 4 Hologram phases on the odd annular zones of the transmitted right-handed (a1) and left-handed (b1) circularly polarized light under the left-handed circularly polarized light, and the corresponding output phase distributions along the  $x$ -direction (c1) and  $y$ -direction (d1) under the  $x$ - and  $y$ -linearly polarized lights, respectively. The corresponding geometric phase is shown in Fig. (e1). The hologram phase on the even zones of the transmitted right-handed (a2) and left-handed (b2) circularly polarized light under the left-handed circularly polarized light, and the corresponding output phase distributions along the  $x$ -direction (c2) and  $y$ -direction (d2) under the  $x$ - and  $y$ -linearly polarized lights, respectively. The corresponding geometric phase is shown in Fig. (e2)

任意轴向位置  $z$  处的矢量衍射场能通过式(3)和式(4)<sup>[32]</sup>所示的矢量角谱理论计算得到。

$$\begin{bmatrix} A_x(f_x, f_y) \\ A_y(f_x, f_y) \end{bmatrix} = \iint_{-\infty}^{\infty} \begin{bmatrix} E_{xi}(x, y, 0) \\ E_{yi}(x, y, 0) \end{bmatrix} \exp[-i2\pi(f_x x + f_y y)] dx dy, \quad (3)$$

$$\begin{bmatrix} E_x(x, y, z) \\ E_y(x, y, z) \\ E_z(x, y, z) \end{bmatrix} = \iint_{-\infty}^{\infty} \begin{bmatrix} A_x(f_x, f_y) \exp(i2\pi f_z z) \\ A_y(f_x, f_y) \exp(i2\pi f_z z) \\ -\frac{f_x A_x(f_x, f_y) + f_y A_y(f_x, f_y)}{f_z} \exp(i2\pi f_z z) \end{bmatrix} \exp[i2\pi(f_x x + f_y y)] df_x df_y, \quad (4)$$

式中:  $E_{xi}(x, y, 0)$  和  $E_{yi}(x, y, 0)$  分别表示入射电场在  $x$  和  $y$  方向的偏振分量;  $A_x(f_x, f_y)$  和  $A_y(f_x, f_y)$  分别表示

上述电场分量的角谱;  $f_x, f_y, f_z$  ( $f_z = \sqrt{1/\lambda^2 - f_x^2 - f_y^2}$ ) 分别表示频率沿着  $x$ 、 $y$  和  $z$  方向的分量, 波长  $\lambda$  等于 633 nm。

为了模拟实际超表面的衍射光场分布,用图 2(b)~(e)中不同尺寸超原子的相位和透过率数据库去匹配图 4(c1)、(d1)和图 4(c2)、(d2)中环形区上单个像素的相位和振幅。根据所有对应位置匹配的超原子的传输相位和图 4(e1)、(e2)中的几何相位计算超表面实际转化的左旋和右旋圆偏振光的复振幅。最后,通过圆偏振光实际复振幅的  $x$  和  $y$  偏振分量以及衍射公式(3)~(4)计算焦平面的衍射光场分布。由于超原子的透过率、相位与实际期望的振幅、相位有一定差别,可能会导致傅里叶全息焦平面中心区出现高强度的亮点,从而使得全息像不能显现。为了去除透射左旋圆偏振光全息图像中心亮点的干扰,将分布在尺寸为  $16.5 \mu\text{m} \times 16.5 \mu\text{m}$  中心区域的所有实际光强全部设置为 0,相当于在物理上用一个不透光的方屏挡

掉了中央零级衍射,从而得到了图 5(c)所示的 QR 码图像。图 5 是仿真得到的设计距离  $z=14.1 \text{ mm}$  处的全息图像。图中横纵轴分别表示  $x$  和  $y$  方向的尺寸。图 5(a)展示了使用左旋圆偏振入射光时手机相机无法识别传输的 QR 码强度分布。但如图 5(b)所示,当滤出透射的右旋圆偏振光时,手机相机就可以识别计算得到 QR 码强度分布。解密信息对应于图 3(b1)中的振幅型全息图,并且最终的解密信息可以通过振幅型全息图透过率函数的傅里叶变换得到。此外,如图 5(c)所示,通过滤出透射的左旋圆偏振光,也可以识别计算得到 QR 码强度分布。在这种情况下,解密信息对应于图 3(b2)中的相位型全息图,并且最终的解密信息可以通过相位型全息图透过率函数的傅里叶变换得到。

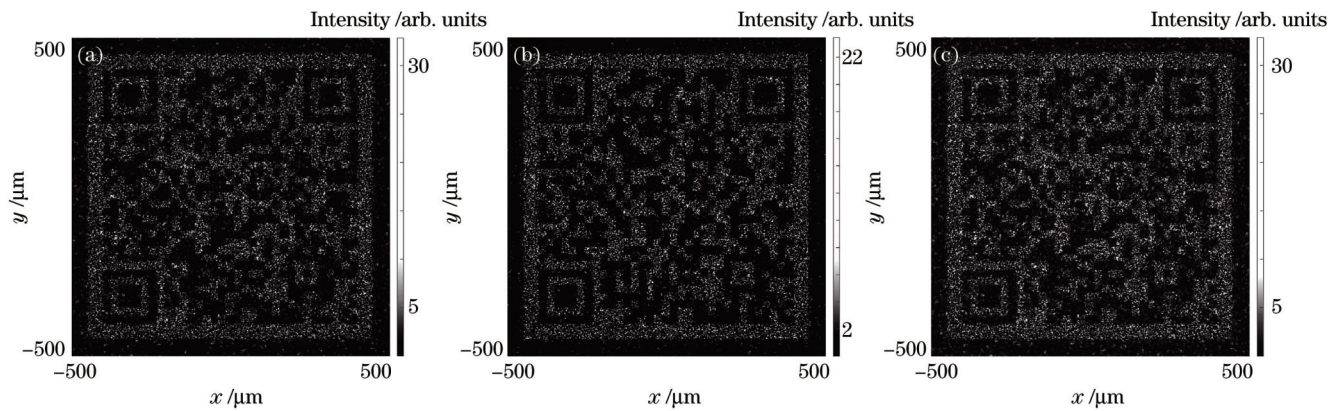


图 5 在左旋圆偏振光入射下,透射的混合圆偏振光(a)、右旋圆偏振光(b)和左旋圆偏振光(c)在设计距离  $z=14.1 \text{ mm}$  处的仿真全息图像

Fig. 5 Simulated holographic images at the designed distance of  $z=14.1 \text{ mm}$  for the transmitted hybrid circularly polarized light, right-handed circularly polarized light and left-handed circularly polarized light under the left-handed circularly polarized incident light, respectively

## 4 结 论

笔者通过将两种类型的超表面波带片集成到单个自旋复用介质超表面中实现了远场偏振全息加密。具体来说,将振幅型奇偶环形区域作为超表面的振幅,将透射的右旋/左旋圆偏振光的相位全息图分别设计为奇数和偶数波带片的相位。研究结果表明,只有在滤出单个圆偏振状态时才能解密加密信息。使用 QR 码和振幅型/相位型全息图可以进一步提高信息的安全性。所提超表面在数据存储和信息加密方面具有潜在应用。

## 参 考 文 献

- [1] Yoon G, Lee D, Nam K T, et al. Crypto-display in dual-mode metasurfaces by simultaneous control of phase and spectral responses[J]. ACS Nano, 2018, 12(7): 6421-6428.
- [2] Jang J, Jeong H, Hu G W, et al. Tunable metasurfaces: Kerker-conditioned dynamic cryptographic nanoprints[J]. Advanced Optical Materials, 2019, 7(4): 1970016.
- [3] Luo X H, Hu Y Q, Li X, et al. Integrated metasurfaces with microprints and helicity-multiplexed holograms for real-time optical encryption[J]. Advanced Optical Materials, 2020, 8(8): 1902020.
- [4] Khorasaninejad M, Chen W T, Devlin R C, et al. Metamaterials at visible wavelengths: diffraction-limited focusing and subwavelength resolution imaging[J]. Science, 2016, 352(6290): 1190-1194.
- [5] Chen W T, Zhu A Y, Sanjeev V, et al. A broadband achromatic metamaterial for focusing and imaging in the visible[J]. Nature Nanotechnology, 2018, 13(3): 220-226.
- [6] Yao J, Lin R, Chen M K, et al. Integrated-resonant metadevices: a review[J]. Advanced Photonics, 2023, 5(2): 024001.
- [7] Huang L L, Chen X Z, Mühlenbernd H, et al. Three-dimensional optical holography using a plasmonic metasurface[J]. Nature Communications, 2013, 4: 2808.
- [8] Zheng G X, Mühlenbernd H, Kenney M, et al. Metasurface holograms reaching 80% efficiency[J]. Nature Nanotechnology, 2015, 10(4): 308-312.
- [9] Ding X M, Wang Z C, Hu G W, et al. Metasurface holographic image projection based on mathematical properties of Fourier transform[J]. PhotoniX, 2020, 1(1): 16.
- [10] Wen D D, Cadusch J J, Meng J J, et al. Light field on a chip: metasurface-based multicolor holograms[J]. Advanced Photonics, 2021, 3(2): 024001.
- [11] Kim J, Seong J, Yang Y, et al. Tunable metasurfaces towards versatile metamaterials and metaholograms: a review[J]. Advanced Photonics, 2022, 4(2): 024001.

- [12] Wang L, Kruk S, Koshelev K, et al. Nonlinear wavefront control with all-dielectric metasurfaces[J]. *Nano Letters*, 2018, 18(6): 3978-3984.
- [13] Reineke B, Sain B, Zhao R Z, et al. Silicon metasurfaces for third harmonic geometric phase manipulation and multiplexed holography [J]. *Nano Letters*, 2019, 19(9): 6585-6591.
- [14] Yang G H, Li Z X, Kang Q L, et al. Enhanced magnetic Lorentz force second harmonic generation originating from a double-resonances plasmonic metasurface[J]. *Journal of Physics D: Applied Physics*, 2021, 54(17): 175110.
- [15] di Leonardo R, Ianni F, Ruocco G. Computer generation of optimal holograms for optical trap arrays[J]. *Optics Express*, 2007, 15(4): 1913-1922.
- [16] Mu Y H, Zheng M Y, Qi J R, et al. A large field-of-view metasurface for complex-amplitude hologram breaking numerical aperture limitation[J]. *Nanophotonics*, 2020, 9(16): 4749-4759.
- [17] Zhao R Z, Huang L L, Wang Y T. Recent advances in multi-dimensional metasurfaces holographic technologies[J]. *PhotonIX*, 2020, 1(1): 1-24.
- [18] Zang X F, Dong F L, Yue F Y, et al. Polarization encoded color image embedded in a dielectric metasurface[J]. *Advanced Materials*, 2018, 30(21): 1707499.
- [19] Deng L G, Deng J A, Guan Z Q, et al. Malus-metasurface-assisted polarization multiplexing[J]. *Light: Science & Applications*, 2020, 9: 101.
- [20] Ren H R, Shao W, Li Y, et al. Three-dimensional vectorial holography based on machine learning inverse design[J]. *Science Advances*, 2020, 6(16): eaaz4261.
- [21] Deng Z L, Deng J H, Zhuang X, et al. Diatomic metasurface for vectorial holography[J]. *Nano Letters*, 2018, 18(5): 2885-2892.
- [22] Bao Y J, Ni J C, Qiu C W. A minimalist single-layer metasurface for arbitrary and full control of vector vortex beams[J]. *Advanced Materials*, 2020, 32(6): 1905659.
- [23] Lane S, Vagin S, Wang H, et al. Wide-gamut lasing from a single organic chromophore[J]. *Light: Science & Applications*, 2018, 7: 101.
- [24] Yang H, He P, Ou K, et al. Angular momentum holography via a minimalist metasurface for optical nested encryption[J]. *Light: Science & Applications*, 2023, 12(1): 79.
- [25] Zhou H Q, Sain B, Wang Y T, et al. Polarization-encrypted orbital angular momentum multiplexed metasurface holography[J]. *ACS Nano*, 2020, 14(5): 5553-5559.
- [26] Zhao R Z, Xiao X F, Geng G Z, et al. Polarization and holography recording in real- and  $k$ -space based on dielectric metasurface[J]. *Advanced Functional Materials*, 2021, 31(27): 2100406.
- [27] Zhao R Z, Li X, Geng G Z, et al. Encoding arbitrary phase profiles to 2D diffraction orders with controllable polarization states [J]. *Nanophotonics*, 2023, 12(1): 155-163.
- [28] Yoon G, Jang J, Mun J, et al. Metasurface zone plate for light manipulation in vectorial regime[J]. *Communications Physics*, 2019, 2: 156.
- [29] Hu Y F, Liu X, Jin M K, et al. Dielectric metasurface zone plate for the generation of focusing vortex beams[J]. *PhotonIX*, 2021, 2 (1): 10.
- [30] Yue Z, Li J T, Li J E, et al. Terahertz metasurface zone plates with arbitrary polarizations to a fixed polarization conversion[J]. *Opto-Electronic Science*, 2022, 1(3): 210014.
- [31] Yuan Y Y, Sun S, Chen Y, et al. A fully phase-modulated metasurface as an energy-controllable circular polarization router [J]. *Advanced Science*, 2020, 7(18): 2001437.
- [32] Ciattoni A, Crosignani B, di Porto P. Vectorial free-space optical propagation: a simple approach for generating all-order nonparaxial corrections[J]. *Optics Communications*, 2000, 177(1/2/3/4/5/6): 9-13.

## Far-Field Polarized Holographic Encryption by Metasurface Zone Plates

Xia Tian, Xie Zhenwei\*, Yuan Xiaocong\*\*

*Nanophotonics Research Centre, Institute of Microscale Optoelectronics & State Key Laboratory of Radio Frequency Heterogeneous Integration, Shenzhen University, Shenzhen 518060, Guangdong, China*

### Abstract

**Objective** Metasurfaces have flexible polarization manipulation functions; however, a lens must be added to obtain the desired far-field-polarized holographic images. This study demonstrates a novel far-field polarization holographic encryption method using flexible polarization manipulation and the focusing capabilities of metasurface zone plates. Two spin-multiplexed metasurface zone plates are integrated into a single metasurface device, where the amplitude (right-handed circular polarization conversion rate) of the metasurface is used to encode the odd and even annular regions of the zone plates, and its phase modulation is utilized to encode two holograms of the transmitted right and left circularly polarized light. Additionally, QR codes and amplitude-only/phase-only holograms are used to hide encrypted information and improve data security. The proposed encryption technology is expected to enhance data security and privacy protection and promote the development of optical information encryption and high-density data storage.

**Methods** The metasurface consisted of odd and even zones of a metasurface zone plate. When left-handed circularly polarized light is incident on the surface, the odd and even zones transform the light into right- and left-handed circularly polarized light, respectively. The polarization conversion efficiencies are 100% and 0% for the odd and even zones, respectively. For the odd zones, the amplitude of the transformed right-handed circularly polarized light is equal to one. For the even zones, the amplitude of the transformed left-handed circularly polarized light is also one. Therefore, the amplitudes of the odd and even zones can be considered amplitude-only odd and even Fresnel zone plates, respectively. In addition, the phases of the odd and even zones were designed as holograms corresponding to right- and left-handed circularly polarized light, respectively (Fig. 2). Thus, the two types of holograms have their respective holographic images in the same focal plane of the amplitude-only odd and even Fresnel zone plates. However, because the images overlapped, the desired encrypted holographic images could not be identified. Therefore, filtering out the right- or left-handed circular polarization can decrypt the corresponding encrypted holographic images.

**Results and Discussions** We use a QR code-generating website to create QR codes that correspond to amplitude-only and phase-only holograms. We then apply the GS algorithm, based on the Fourier transform relationship, to generate either an amplitude-only or a phase-only hologram. Subsequently, the amplitude-only hologram and phase-only hologram undergo Fourier transform to produce an encrypted intensity profile and an encrypted intensity distribution, respectively (Fig. 3). The odd and even zones refer to the designed holograms corresponding to the output right- and left-handed circular polarization components, respectively. Although transmitted phases exist for the left and right circular-polarization components in the odd and even zones, respectively, the amplitudes of these phases are essentially zero and can be disregarded (Fig. 4). To simulate the diffraction light field distribution of actual metasurfaces, we match the phase and amplitude of a single pixel in the annular region in Figs. 4(c1) and (d1) and Figs. 4(c2) and (d2) to the transmitted phase and transmission rate of all corresponding positions of the metasurface using the phase and transmission rate databases of differently sized meta-atoms in Figs. 2(b)–(e). The complex amplitudes of the left- and right-circularly polarized light transformed by the metasurface are calculated using the transmitted phases and geometric phases in Figs. 4(e1) and (e2). Finally, the diffraction light field distribution at the focal plane is calculated using the  $x$ - and  $y$ -polarization components of the actual complex amplitude of the circularly polarized light and diffraction formula (3) and (4). Because the transmission rate and phase of the meta-atoms differ from the expected amplitude and phase, the center of the Fourier hologram focal plane may have a high-intensity bright spot, making it impossible to display the hologram image. To eliminate the disturbance of the bright spot in the hologram image of the transmitted left-circularly polarized light, we set all values in the central area of the actual light intensity distribution with a size of  $16.5 \mu\text{m} \times 16.5 \mu\text{m}$  to 0, which is equivalent to physically blocking the central zero-order with an opaque square screen, thus obtaining the QR code image represented in Fig. 5. Figure 5 shows the simulation results representing the hologram image at a simulated distance of  $z=14.1 \text{ mm}$ . The transmitted QR code intensity profile could not be recognized by the phone camera when the left-handed circularly polarized incident light is used. However, when the transmitted right-handed circularly polarized light is filtered out, the calculated QR code intensity profile can be identified using a phone camera. The decrypted information corresponds to the amplitude-only hologram, and we obtain the final decryption information by performing a Fourier transform on the amplitude-only hologram transmittance function. Moreover, by filtering out the transmitted left-circularly polarized light, the calculated QR code intensity profile can be identified using a phone camera. In this case, the decrypted information corresponds to a phase-only hologram, and we obtain the final decryption information using the Fourier transform of the phase-only hologram transmittance function (Fig. 5).

**Conclusions** We introduce a novel approach for achieving far-field polarized holography encryption by integrating two types of metasurface zone plates into a single dielectric spin-multiplexed metasurface. Specifically, we utilized amplitude-only odd- and even-zone plates for their amplitudes and phase holograms of the transmitted right- and left-circularly polarized light for their phases. Our results demonstrate that encrypted information can only be decrypted when a single circularly polarized state is filtered. The use of QR codes and amplitude-only/phase-only holograms further improves information security. The proposed metasurface technology has potential applications in the fields of data storage and information encryption.

**Key words** optics at surface; metasurface zone plate; far-field polarized holography encryption; QR code; holography